TU Delft

Delft University of Technology

Saturated transverse permeability of unidirectional rovings for pultrusion
The effect of microstructural evolution through compaction

Yuksel, Onur; Caglar, Baris; Broggi, Guillaume; Michaud, Véronique; Akkerman, Remko; Baran, Ismet

DOI
10.1002/pc.28171

Publication date
2024

Document Version
Final published version

Published in
Polymer Composites

Citation (APA)
Yuksel, O., Caglar, B., Broggi, G., Michaud, V., Akkerman, R., & Baran, I. (2024). Saturated transverse permeability of unidirectional rovings for pultrusion: The effect of microstructural evolution through compaction. *Polymer Composites*, *45*(7), 5935-5952. https://doi.org/10.1002/pc.28171

Important note
To cite this publication, please use the final published version (if applicable).
Please check the document version above.

Copyright
Other than for strictly personal use, it is not permitted to download, forward or distribute the text or part of it, without the consent of the author(s) and/or copyright holder(s), unless the work is under an open content license such as Creative Commons.

Takedown policy
Please contact us and provide details if you believe this document breaches copyrights.
We will remove access to the work immediately and investigate your claim.

This work is downloaded from Delft University of Technology.
For technical reasons the number of authors shown on this cover page is limited to a maximum of 10.

Check for updates

Received: 2 October 2023 | Revised: 10 January 2024 | Accepted: 12 January 2024

DOI: 10.1002/pc.28171

RESEARCH ARTICLE

Polymer COMPOSITES WILEY

Saturated transverse permeability of unidirectional rovings for pultrusion: The effect of microstructural evolution through compaction

Onur Yuksel[1,2] | **Baris Caglar**[2] | **Guillaume Broggi**[2,3] | **Véronique Michaud**[3] | **Remko Akkerman**[1] | **Ismet Baran**[1]

[1]Faculty of Engineering Technology, University of Twente, Enschede, the Netherlands

[2]Faculty of Aerospace Engineering, Delft University of Technology, Delft, the Netherlands

[3]Laboratory for Processing of Advanced Composites (LPAC), Institute of Materials (IMX), Faculty of Engineering (STI), Ecole Polytechnique Fédérale de Lausanne (EPFL), Lausanne, Switzerland

Correspondence

Remko Akkerman, Faculty of Engineering Technology, University of Twente, Enschede 7500AE, the Netherlands.
Email: r.akkerman@utwente.nl

Baris Caglar, Faculty of Aerospace Engineering, Delft University of Technology, Kluyverweg 1, Delft 2629HS, the Netherlands.
Email: b.caglar@tudelft.nl

Funding information

Danish Council for Independent Research | Technology and Production Sciences (DFF/FTP), Grant/Award Number: DFF-6111-00112; Swiss National Science Foundation, Grant/Award Number: SNF-182669

Abstract

The transverse permeability of roving/tow-based fiber reinforcement is of great importance for accurate flow modeling in the pultrusion process. This study proposes an experimental approach to characterize the roving-based fiber beds' permeability under different compaction conditions. The experimental permeability results of thick roving-based preforms were reported and compared with the permeability values of roving-based preforms in the literature. A representative preform was infused under vacuum conditions. Its thickness was varied to replicate the different compaction values observed in permeability tests. Micrographs were then collected from it and analyzed to highlight the microscale transformations caused by processing/compaction on the fiber arrangement. The analysis revealed that compaction resulted in the reorganization of filaments along the direction of the applied compaction. Overall, the uniformity of the spatial filament distribution, i.e., the homogeneity within the fibrous domain, increased with increasing compaction. Furthermore, the microstructural analysis demonstrated transverse anisotropy within the tested domains, indicating that the obtained permeability results represented an upper boundary. In addition to the experimental analyses, various transverse permeability models, which were developed based on recently introduced statistical descriptors of fiber distribution, were evaluated by using the statistical descriptors extracted from the analyzed cross-sections. Among these models, the one correlating the second neighbor fiber distance with apparent permeability exhibited good agreement with the experimental results.

Highlights

- Transverse permeability measurement of a roving-based reinforcement was presented.
- The influence of compaction on the microstructure was investigated at the filament level.

This is an open access article under the terms of the Creative Commons Attribution License, which permits use, distribution and reproduction in any medium, provided the original work is properly cited.
© 2024 The Authors. *Polymer Composites* published by Wiley Periodicals LLC on behalf of Society of Plastics Engineers.

- Filament distribution in a pultruded profile was analyzed by using statistical descriptors.
- The results of the experiments and the models in the literature were compared.
- The correlation between microstructural features and apparent permeability was discussed.

KEYWORDS

microstructural analysis, permeability, pultrusion, vacuum infusion

1 | INTRODUCTION

1.1 | Motivation

Resin injection pultrusion (RIP) is a continuous process for manufacturing fiber-reinforced polymer composites. It consists of the impregnation of dry fibers with resin in an injection box and, subsequently, the solidification of the impregnated fibrous material in a heated die that is adjacent to the injection box.[1] The solidified profile is pulled continuously and cut to the desired length afterward to produce pultruded parts with constant cross-sections.

Good impregnation is crucial for the quality of pultruded parts. High-quality composite parts can be produced by complete impregnation of the fibers, which can be achieved by choosing suitable process parameters considering the corresponding material properties. Process parameters such as pulling speed and die temperature can be optimized to obtain full impregnation and minimum porosity using numerical process simulations.[2–4] Permeability characteristics of the fiber reinforcement (in addition to the resin properties such as the viscosity and the cure kinetics[5,6]) are key to such process simulations, which are known to be strongly related to fiber distribution.

In pultrusion, the most commonly used type of reinforcement is a unidirectional (UD) roving assembled from a number of filaments. During the pultrusion process, multiple rovings are simultaneously fed through guiding plates to the die or the injection box for the resin bath pultrusion or the RIP, respectively. This results in an uncontrolled distribution of rovings and filaments at the meso- and micro-scale.[7–9] Due to the lack of control in roving distribution, inter-roving pore spaces form irregularly over the cross-section of the pultruded profile. In addition to the mesoscale irregularity, an inevitable non-uniformity in filament distribution forms at the microscale. In Figure 1, the micrographs taken from a pultruded part depict the resin-rich regions, filament distribution non-uniformity, and porosity. The resin-rich regions shown in this figure can be considered as the pore spaces during the impregnation process. An in-depth, three-dimensional (3D) analysis of non-uniformity in fiber distribution and voids in pultruded parts can be found in the study of Baran et al.[10]

The local variability in fiber distribution and the pore spaces, which turn into resin-filled regions after processing, as shown in Figure 1, result in a complex permeability field. This complex field needs to be investigated deeply to provide an accurate estimation of the impregnation kinetics and quality.

Permeability measurements typically show a large scatter in results even under strictly controlled experimental conditions, as exemplified in international benchmarks even for standard fabrics.[11–14] The roving-based fiber beds additionally lack the structural integrity of fabrics, which makes the permeability characterization of such systems challenging. In addition to the experimental challenges, roving-based fiber beds have distinctive microstructural evolution through compaction due to the lack of internal confinements such as interlacing structures or stitching-like transverse support. Therefore, it is crucial to develop a repeatable and controllable permeability characterization test procedure for roving-based fiber beds, which is representative of the microstructure found in pultrusion. The goal of this work is to develop an experimental campaign consisting of a permeability measurement method for roving-based preforms and to investigate the microstructure of the preform under different levels of compaction at the length scale of a filament. This experimental campaign and the complementary permeability analysis on the investigated microstructures shed light on the relationship between processing-structure-property. These terms, respectively, represent compaction-fiber distribution-permeability for the present work. To fulfill this goal, we carried out comprehensive work to investigate the transverse permeability of a roving-based system considering its dependency on fiber distribution.

Firstly, we designed a methodology for the transverse permeability measurements of roving-based fiber beds used in the pultrusion process. The transverse permeability was measured within a modified 1D permeameter at different compaction levels corresponding to different fiber volume fraction (V_f) values. Secondly, we prepared

15480569, 0, Downloaded from https://4spepublications.onlinelibrary.wiley.com/doi/10.1002/pc.28171 by Cochrane Netherlands, Wiley Online Library on [22/02/2024]. See the Terms and Conditions (https://onlinelibrary.wiley.com/terms-and-conditions) on Wiley Online Library for rules of use; OA articles are governed by the applicable Creative Commons License

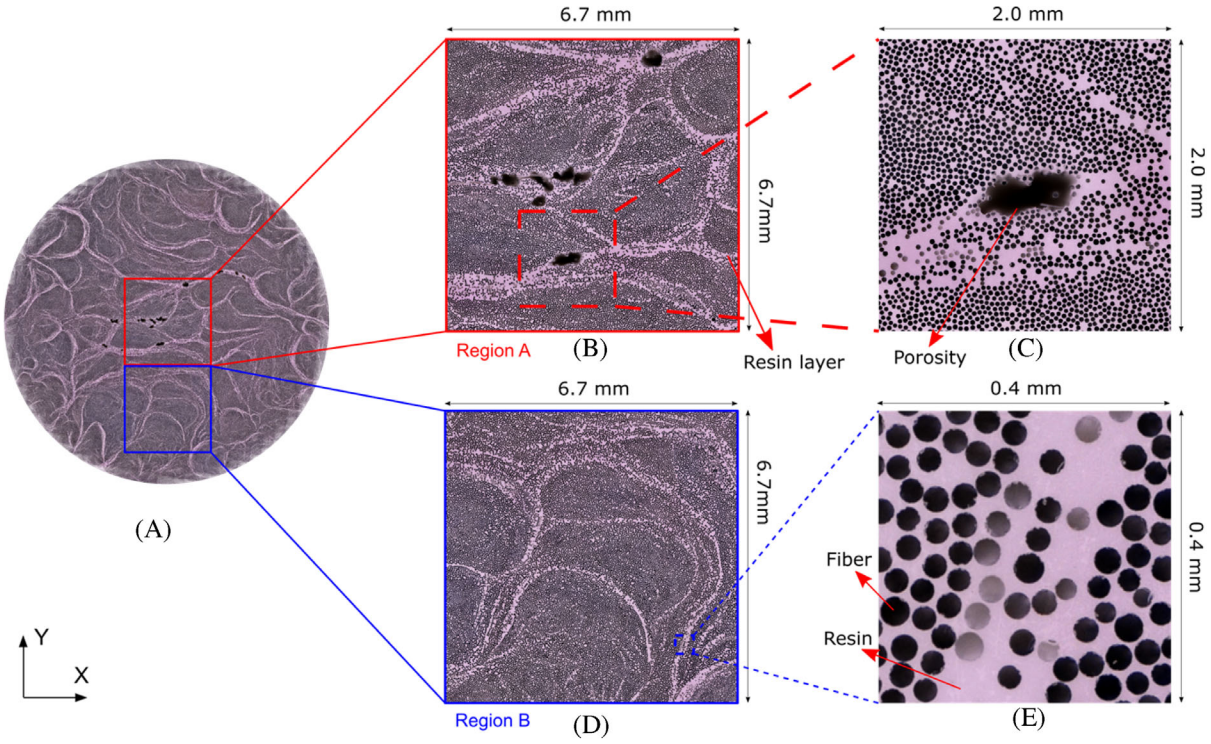

FIGURE 1 Representative micrographs from a pultruded profile. Whole cross-section of a pultruded bar with 25 mm of diameter (A) and magnified cross-sections (B–E). Region A is shown in the red square in (A, B). Region B is shown in the blue square in (A, D).

a similar preform in a vacuum infusion process, infusing a thermosetting resin to fix the fibers. The internal structure of the cured sample was captured via optical light microscopy, and the fibers were detected using image processing. The fiber distribution in the preform was characterized at different compaction levels and statistically analyzed. The fiber distribution in these cross-sections was also compared with the fiber distribution in a commercial pultruded part to validate the method. Furthermore, the effect of fiber distribution through the cross-section on transverse permeability was estimated using existing fiber distribution statistics-based models published in the literature, and their suitability for permeability characterization of roving-based systems was investigated.

1.2 | Background

Only a limited number of studies have measured the transverse permeability of a roving-based fiber bed as found in pultrusion processes, that is, without any transverse support such as stitch or weave. Figure 2 depicts some of these set-ups schematically. As one of the earlier examples for this purpose, Bates et al.[15] designed a so-called "compression permeability set-up" for roving-based preforms which is a version of through-thickness permeability (TTP) set-up (see Figure 2B). Recently with a similar approach, Werlen et al.[16] designed a permeability rig modified with an adapter that has an opening with the desired shape. Both of these set-ups were designed to test straight and side-by-side stacked tows/rovings in a rectangular prism-shaped testing space. To measure the transverse permeability of rovings, Schell et al.[17] designed a permeameter in which the straightness and the alignment of fibers were set by winding them around a frame. In References 18, 19, a radial flow test within a closed mold with a moving upper plate (see Figure 2C) was used to measure the in-plane permeability of UD and air-texturized rovings, as the latter consists of wavy fibers made by processing UD rovings. These roving-based fiber beds in References 18, 19 were held in place by fiber guides, as in pultrusion. Wu et al.[20] similarly used radial flow, but they wound the roving instead of using roving guides. The fluid flows radially into the reinforcement, and the roving in this study was wound around the winding direction, which is perpendicular to the flow plane. Each of these experimental methodologies has a distinctive sample preparation procedure that results in quite different microstructures in the sense of inter-tow regions' formation.

Recent studies proposed experimental characterization strategies to assess the permeability of tows with microstructural analysis. Zarandi et al.[21] measured the permeability of roving-based preforms with a relatively

15480569, 0, Downloaded from https://4spepublications.onlinelibrary.wiley.com/doi/10.1002/pc.28171 by Cochrane Netherlands, Wiley Online Library on [22/02/2024]. See the Terms and Conditions (https://onlinelibrary.wiley.com/terms-and-conditions) on Wiley Online Library for rules of use; OA articles are governed by the applicable Creative Commons License

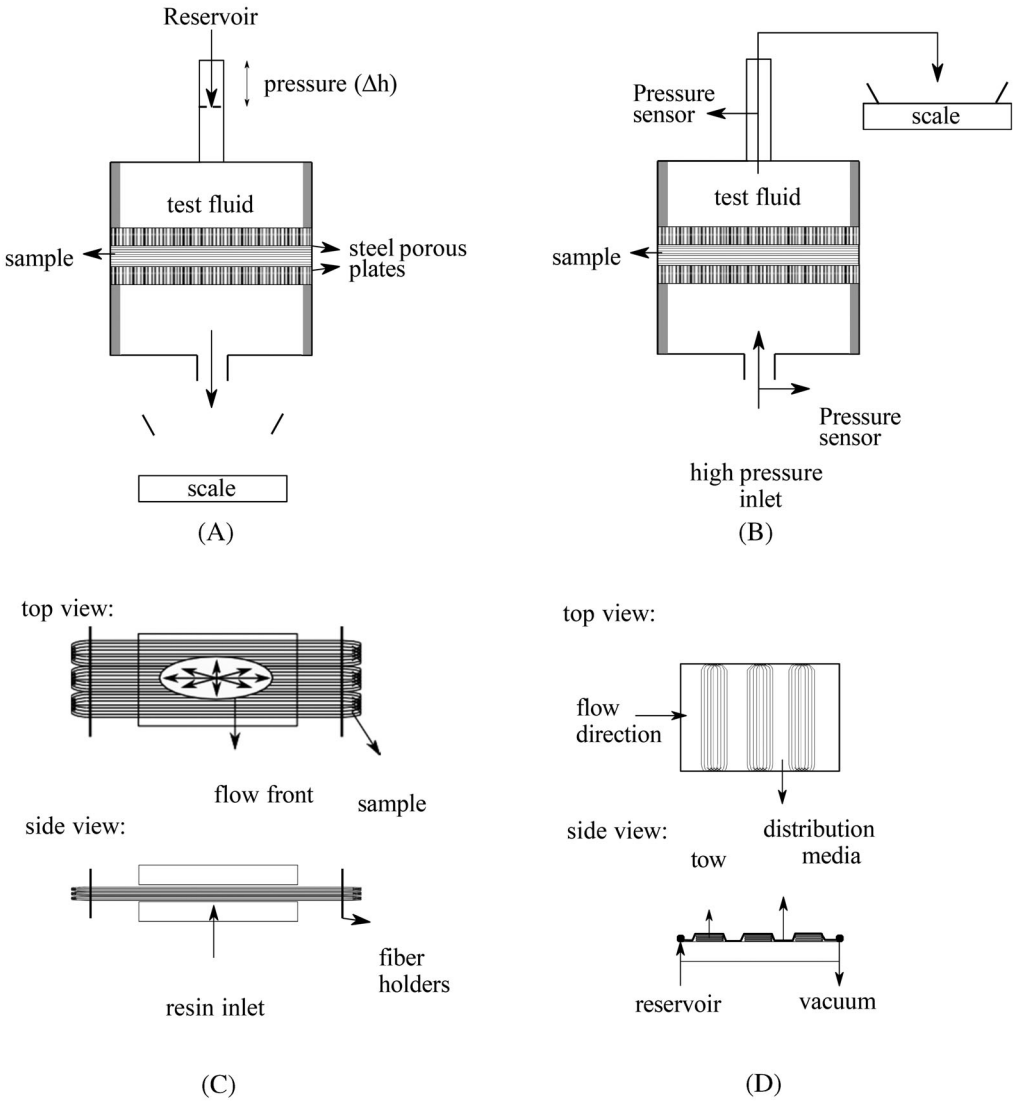

FIGURE 2 Schematic representations of the permeability set-ups for tows/rovings. (A) Gravity-driven falling-head type permeameter, (B) pressure driven 1D permeameter, (C) in-plane permeability set-up for radial flow tests, (D) permeability set-up designed as a vacuum-assisted resin transfer molding process with flexible top mold.

simple gravity-driven falling head permeameter (see Figure 2A) and took cross-sectional microscopy images of similarly prepared cured samples. The tow permeability, i.e., intra-tow permeability, was focused on by ensuring high fiber volume fraction. It was shown that the experimental results were in a good agreement with the numerically estimated permeability values, which were calculated within the representative volume elements (RVEs) collected from the analyzed cross-sections. Godbole et al.[22] proposed a novel method for measuring the permeability of rovings/tows involving vacuum-assisted resin transfer molding (VARTM), with a vacuum bag serving as a flexible upper mold (see Figure 2D). The fiber distribution was analyzed in a tested tow, and a semi-analytical method was proposed to understand the influence of the microstructure on tow permeability.

In addition to the experimental studies, both theoretical and numerical approaches attempted to estimate the transverse permeability of fibrous structures. A well-known expression for the permeability of fiber beds was developed by Gebart[23] with the assumption of a uniform fiber distribution. The expression for the transverse permeability of hexagonally or quadratically distributed fibers, Equation (1), is as follows;

$$K_{\perp} = C_1 \cdot \left(\sqrt{\frac{V_{f\max}}{V_f}} - 1 \right)^{2.5} \cdot r^2, \qquad (1)$$

where C_1 is a fiber arrangement dependent parameter that is equal to $\left(\frac{16}{9\pi\sqrt{6}}\right)$ for the hexagonal distribution, and $\left(\frac{16}{9\pi\sqrt{2}}\right)$ for the quadratic distribution. The term,

15480569, 0, Downloaded from https://4spepublications.onlinelibrary.wiley.com/doi/10.1002/pc.28171 by Cochrane Netherlands, Wiley Online Library on [22/02/2024]. See the Terms and Conditions (https://onlinelibrary.wiley.com/terms-and-conditions) on Wiley Online Library for rules of use; OA articles are governed by the applicable Creative Commons License

$V_{f\max}$, is the theoretical maximum fiber volume content, that is equal to 0.907 for the hexagonal distribution and 0.785 for the quadratic distribution. The term V_f is the fiber volume content of the analyzed cross-section, and r is the filament radius.

The statistical analysis of fiber distribution in composite structures confirms that fiber-reinforced polymers do not have a uniform microstructure.[24–27] The spatial distribution of fibers and their non-uniformity can be quantitatively characterized via statistical descriptors. Locally, the non-uniformity of the fiber distribution influences the apparent permeability of regions of interest (ROIs). Moreover, the stochastic nature of the fiber distribution results in a variable apparent permeability value at the macro level.[28,29]

The effect of fiber distribution on the transverse permeability has been investigated in the literature to correlate statistics on fiber distribution with apparent permeability.[28,30–32] It is worth mentioning that these studies have done 2D Stokes flow analysis with Newtonian liquids and without surface tension effects for the saturated permeability estimation. Bechtold et al.[30] proposed using the Morisita index, which is a statistical measure of particle dispersion, to include the effect of fiber agglomeration on apparent permeability estimation. Another commonly used statistical parameter correlated with the apparent permeability is the average nearest fiber distance, which is obtained by averaging the distance of each fiber in the inspected domain to its first, second, or third nearest neighbor. Chen et al.[31] showed that the apparent permeability decreases as the non-uniformity in fiber distribution increases for RVEs with a fiber volume fraction higher than 0.3. Based on 600 simulations, they proposed a correlation between the average closest neighbor fiber distance and apparent permeability:

$$K_{\perp} = K_{\text{hex}} \cdot \left(\frac{\delta_1}{\delta_{\text{hex}}}\right)^{\left(1.51-1.93\cdot\left(1-V_f\right)\right)}, \quad (2)$$

where δ_1 is the average first fiber neighbor distance, δ_{hex} is the corresponding first fiber neighbor distance of uniform hexagonal distribution, and K_{hex} is the corresponding transverse permeability value calculated by using Gebart's expression for the hexagonal distribution. A similar analysis was conducted by Yazdchi et al.[28] using randomly generated RVEs, who proposed a correlation between the average second fiber neighbor distance and apparent permeability,

$$K_{\perp} = 0.2 \cdot \left(0.5 \cdot \overline{\delta_2}\right)^{2.5} \cdot \left(1 - 0.5 \cdot e^{-1.5\cdot\overline{\delta_2}}\right) \cdot d^2, \quad (3)$$

where $\bar{\delta}_2$ is the average second fiber neighbor distance normalized by the average fiber radius, and d is the diameter of one filament. Gommer et al.[32] showed that implementing a realistic fiber distribution into the model is essential, proposing five different statistical descriptors instead of one descriptor to address the scatter in the estimated permeability values.

$$\ln(K_{\perp}) = 6.74 \cdot \overline{\delta_2} - 4.22 \cdot \overline{\delta_3} - 4.77 \cdot \sigma\overline{\delta_2} - 0.1 \cdot \sigma\overline{\delta_3} - 46.6 \cdot V_f, \quad (4)$$

where $\bar{\delta}_2$ and $\bar{\delta}_3$ are the average second and third fiber neighbor distance, normalized by the average radius. $\sigma\bar{\delta}_2$ and $\sigma\bar{\delta}_3$ are the standard deviations of these parameters. The descriptors used in this expression were determined using multiple linear regression analysis conducted on CFD results of 211 different RVEs with fiber volume fractions greater than 0.6. Gommer et al.[32] also presented the comparison between their proposed model and the previously developed expressions presented above for their artificially generated statistically equivalent microstructures.

These studies modeled flow in RVEs with either random or statistics-based fiber distribution. However, the microstructure of a fiber-reinforced composite changes due to compaction during the pultrusion process. Random RVE generation would conceal the segregated cross-sections of roving based systems and the effect of processing-induced microstructural transformation on permeability. Statistics-based RVE generation, on the other hand, should consider the distinctive characteristics of roving-based fiber beds through compaction compared to the fabrics or prepregs due to intra- and inter-roving regions. Therefore, the characteristic microstructural transformation of continuous roving-based fiber beds, which consists of simultaneous reformation of resin-rich layers and filaments during compaction, must be taken into account to estimate the transverse permeability of this type of reinforcement accurately. To the best of the authors' knowledge, no studies have analyzed the compaction-induced microstructural transformation of a thick roving-based fiber bed and its correlation with the experimentally measured transverse permeability.

2 | MATERIALS AND METHODS

2.1 | Materials

A pultrusion-specific 4800 TEX E-glass fiber roving ($\rho_f = 2.55$ g/cm^3) was extracted from an inside-out bobbin and used for the permeability tests and vacuum infusion. The average filament radius was measured as 11 μm.

The test fluid used in the permeability tests was an aqueous solution of polyethylene glycol (Sigma Aldrich, 35 kDa). At a concentration level of 16.7 wt%, its viscosity

15480569, 0, Downloaded from https://4spepublications.onlinelibrary.wiley.com/doi/10.1002/pc.28171 by Cochrane Netherlands, Wiley Online Library on [22/02/2024]. See the Terms and Conditions (https://onlinelibrary.wiley.com/terms-and-conditions) on Wiley Online Library for rules of use; OA articles are governed by the applicable Creative Commons License

was measured to be around 107 mPa.s at room temperature by using a rheometer with a cylindrical Couette geometry. Vacuum grease is used for sealing purposes during testing. It may contaminate the test fluid and alter its viscosity. Viscosity measurements were therefore performed before and after the tests. They showed that there was no significant change in the viscosity of the test fluid before and after the tests.

In addition, a glass fiber-reinforced polyester commercial pultruded part was analyzed to validate our observations with practical applications and varying materials. The average filament radius was measured as 16 μm. The fiber distribution was extracted over a 25 mm diameter cross-section. Two regions were selected for comparison with the vacuum-infused sample. These regions were labeled as "Region A" and "Region B," respectively, indicated by red and blue squares in Figure 1A.

2.2 | Methods

2.2.1 | Permeability measurement

1D saturated permeability setups are commonly used for measuring the transverse permeability of fibrous structures. The experimental practice with this setup is performed by placing a sample consisting of dry fibers between two perforated plates. The test fluid is injected along the through-thickness direction with a constant flow rate or constant pressure to estimate transverse permeability,[33] also known as TTP[34–36] or out-of-plane permeability[14,37] for fabrics. The literature describes that various modifications to the 1D permeability setup have been considered for several different purposes.[38–44] A detailed analysis of the design parameters of the corresponding set-up can be seen in Reference 45.

A 1D permeability set-up was presented by van de Ven et al.[46] for the out-of-plane permeability measurements of carbon fiber fabrics. For this study, the corresponding 1D setup was modified to measure the saturated transverse permeability of a roving-based fiber bed. A schematic representation of the permeameter and the full permeability setup are shown in Figure 3C,D, respectively.

The roving-based fiber beds, called "preform" in the present study, must be prepared in a repeatable and controllable fashion to provide an accurate permeability estimation. Each preform was made of a single roving wound around a hollow stainless steel pin with an outer diameter of 1 cm. As the first step of the preform preparation, the free end of the roving from the bobbin was pulled through the hole on the pin and tacky tape was used to prevent any flow through this hole and the core part of the wound preform. The winding was performed carefully without twisting the roving between perforated plates, as depicted in Figure 3A. During winding, the gap between the perforated plates was controlled and kept at a fixed size of nominally 8 (±1) mm that was close to the width of one roving. After winding each 15 cm section of roving, a 20 N dead weight was used to stretch the roving, as illustrated in Figure 3B. The roving's wound and feeding ends were positioned at a 120° angle in the winding plane to exert a stretching load of 20 N. In the wound preforms, the uniformity of the roving distribution in the radial direction was visually checked. The dry preforms were weighed before the measurements, and their fiber volume content was calculated based on their weights.

The perforated plates of the permeability setup were laser cut from a 10 mm thick stainless steel plate with a diameter of 95 mm, while the perforated part had a diameter of 80 mm. The diameter of each hole was 10 mm. Potential race-tracking from the area between the inner wall of the permeameter and the preform was avoided by sealing the inner walls with vacuum grease (see Figure 3C). Vacuum grease was selected as the sealant as it did not interfere with the height changes of the test domain. This allowed performing multiple measurements using a single sample at different fiber volume fractions by altering the height in between the measurements, and such a modularity would not be possible if we were to opt for an incompressible fixed height spacer as used in References 47, 48.

The permeameter was closed after placing the sample. A linear variable displacement transducer, which was calibrated by putting metal gauge blocks between the porous plates similar to the preforms, was set to measure the thickness of the sample from the moving head pressing on the preform via the perforated plates. The outlet of the permeameter, i.e., the upper surface of the preform, was open to the atmospheric pressure at the beginning (see Figure 3C). The pressure difference induced flow was initiated by pressurizing the pot containing the test fluid with relatively low gauge pressure (0.1 bar) to fill the inlet side of the permeameter and the preform while avoiding flow-induced deformation.[44] Each sample was tested at three different thicknesses (with different V_f), and the air gauge pressure was set to approximately 0.3, 0.6, and 1.0 bar at each thickness level. The inlet and outlet pressures were continuously measured using two different pressure sensors mounted on the inlet port and the outlet port of the permeameter. The flow rate was monitored by continuously weighing the outgoing test fluid with a load cell. An example of a flow rate and pressure drop measurement for one of the preforms for a given thickness level, or V_f, is shown in Figure 3E,F. The apparent permeability was calculated using Darcy's Law,

$$K_{\perp} = \frac{Q \cdot \mu \cdot L}{A \cdot \Delta P}, \tag{5}$$

15480569, 0, Downloaded from https://4spepublications.onlinelibrary.wiley.com/doi/10.1002/pc.28171 by Cochrane Netherlands, Wiley Online Library on [22/02/2024]. See the Terms and Conditions (https://onlinelibrary.wiley.com/terms-and-conditions) on Wiley Online Library for rules of use; OA articles are governed by the applicable Creative Commons License

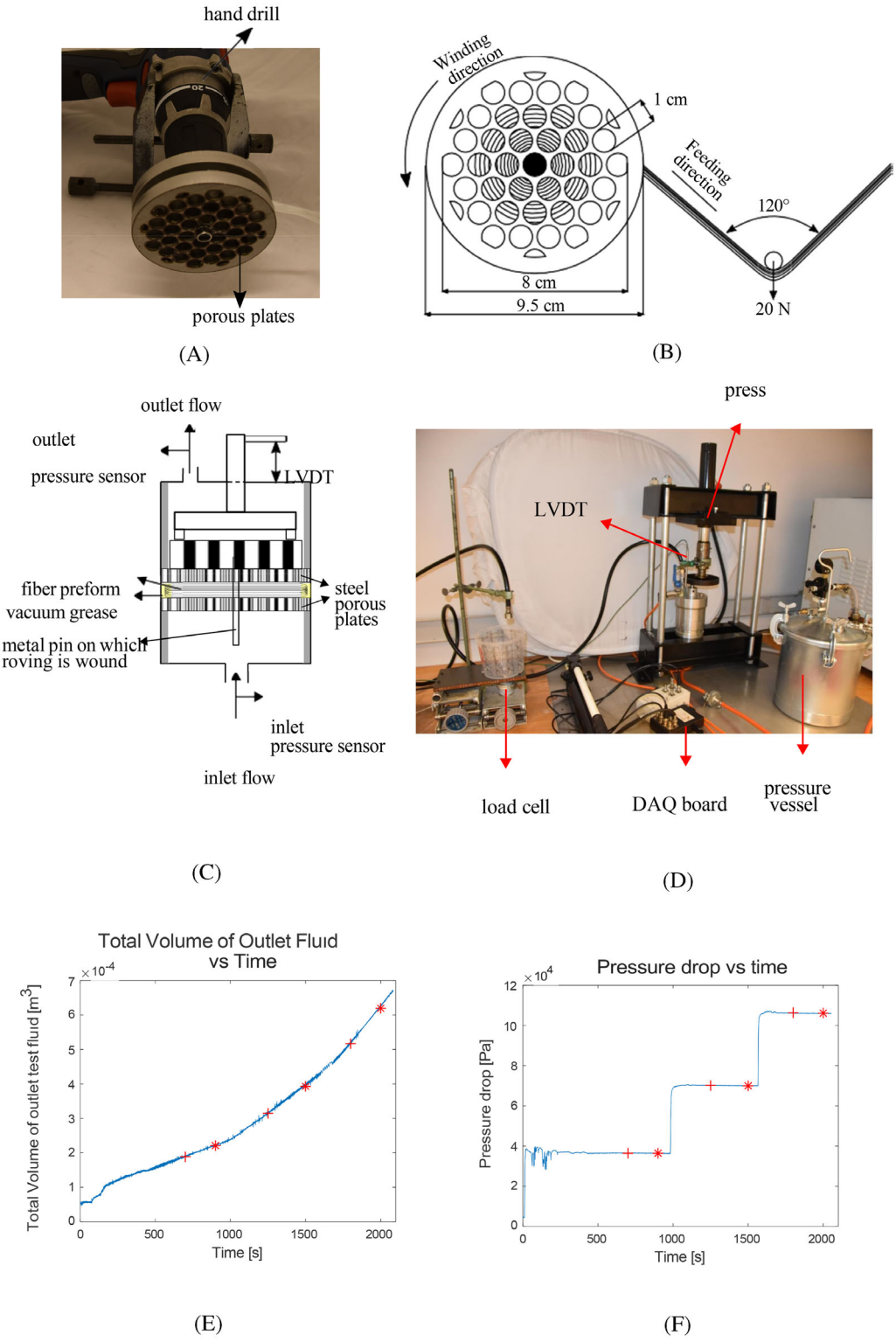

FIGURE 3 The roving was wound around a pin between perforated plates with a hand drill (A). A schematic representation of winding under tension (B). Schematic view of the permeameter (C), permeability test set-up (D). An example of volumetric flow reading during the test (E). An example of pressure drop reading during the test (F).

where Q is the measured volumetric flow rate, μ is the viscosity, L is the length of the gap between the perforated plates, A is the cross-sectional area, and ΔP is the measured pressure drop.

Measurements were conducted on five different preforms in total. Three different V_f values were set for each preform, and three different pressure values were used at each height level. A first-order polynomial was fitted between the natural

15480569, 0, Downloaded from https://4spepublications.onlinelibrary.wiley.com/doi/10.1002/pc.28171 by Cochrane Netherlands, Wiley Online Library on [22/02/2024]. See the Terms and Conditions (https://onlinelibrary.wiley.com/terms-and-conditions) on Wiley Online Library for rules of use; OA articles are governed by the applicable Creative Commons License

logarithm of the apparent permeability (ln (K)) and V_f, using an empirical relation between the permeability and V_f,

$$K_{\perp} = C \cdot \exp\left(-b \cdot V_f\right), \tag{6}$$

where C and b are the fitting constants. For the overall fit, the slope was calculated as the average slope of the individual fitting.

2.3 | Vacuum infusion

A similar preform was prepared by winding a roving on a round base, and a composite specimen was manufactured out of it by vacuum infusion followed by curing to fix the fibers and further investigate the local fiber distribution. A roving thus was attached to and wound around a pin. The pin, in this case, was a vacuum hose instead of a hollow steel pin. The roving was wound between two solid molds, a 1.5 cm thick aluminum plate with a resin inlet aperture, and a 1 cm thick glass plate to observe the flow progress. Before closing the gap between the molds to obtain a vacuum chamber around the dry preform, 1 mm thick glass shims were placed for local thickness adjustment. The dry preform was impregnated with epoxy resin using a vacuum infusion process. The sample preparation steps and a schematic representation of the vacuum chamber are shown in Figure 4A–C. Spacers set the gap between the molds to 9 mm. The thicknesses of two separate zones of the preform were reduced to 8 and 7 mm, respectively, with one and two 1 mm thick glass shims, as shown in Figure 4D–F. Epoxy resin was infused from the middle of the preform. Vacuum pressure was supplied from the outer periphery to impregnate the preform. The cured sample was cut along the blue lines schematically shown in Figure 4D,E, away from the region where the

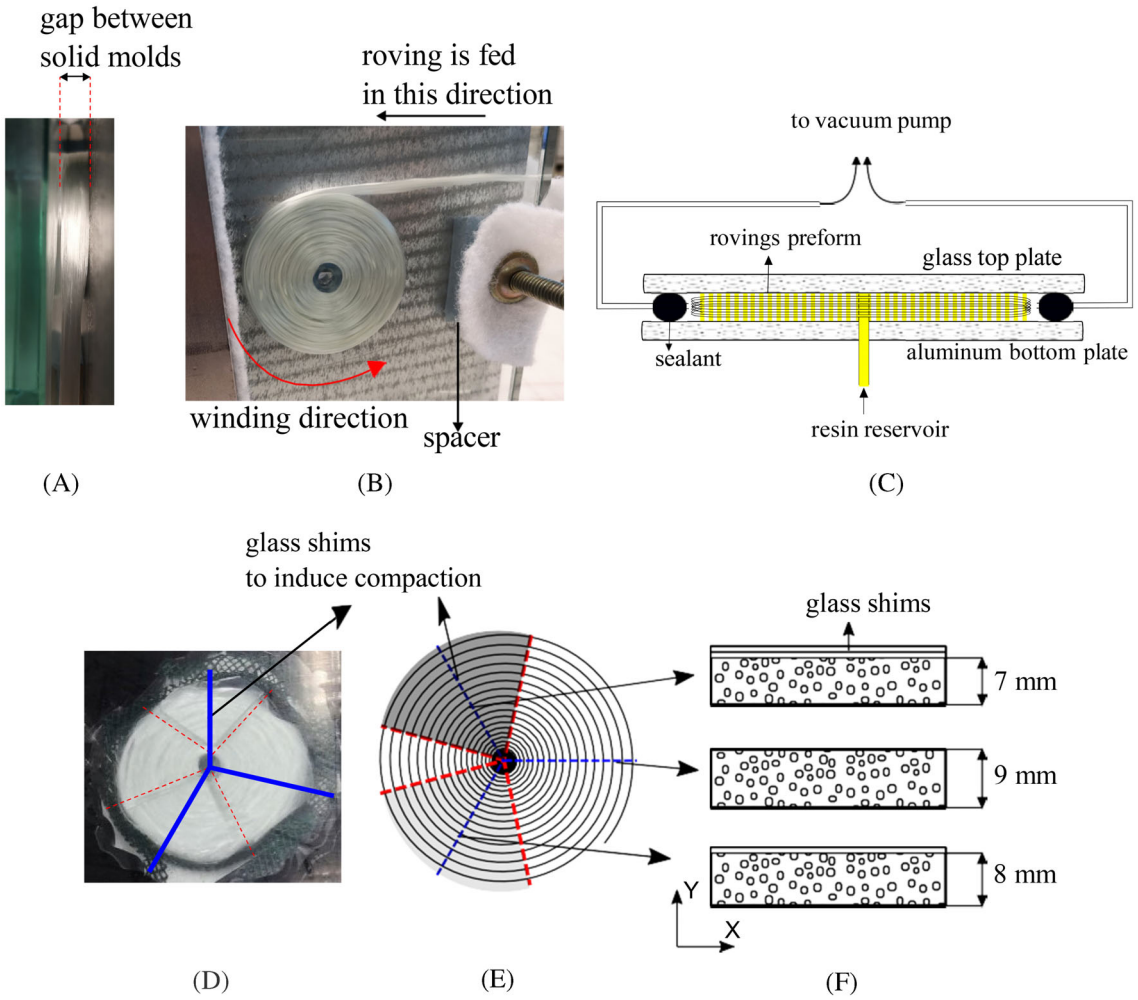

FIGURE 4 Winding process for the vacuum infusion, side view (A), front view (B). Representative schematic view of the vacuum infusion set-up (C). Vacuum chamber with glass shims (D) and its schematic representation (E). Schematic cross-sectional views (F).

15480569, 0, Downloaded from https://4spepublications.onlinelibrary.wiley.com/doi/10.1002/pc.28171 by Cochrane Netherlands, Wiley Online Library on [22/02/2024]. See the Terms and Conditions (https://onlinelibrary.wiley.com/terms-and-conditions) on Wiley Online Library for rules of use; OA articles are governed by the applicable Creative Commons License

V_f is varying, to observe and statistically analyze filament distribution at different compaction levels. These 9, 8, and 7 mm thick cross-sections were labeled "low V_f", "mid V_f", and "high V_f", respectively.

3 | IMAGE PROCESSING AND FIBER DISTRIBUTION STATISTICS

The vacuum-infused preform and the commercial pultruded part were cut using a diamond saw and ground/polished in an automated polishing machine ("Struers Tegramin-30"). The analyzed cross-sections were characterized using a "KEYENCE VHX 5000" optical microscope with a 100–1000× lens. Images were taken with 400× magnification. The estimated pixel density was 2.10 pixel/μm. Each image from the vacuum-infused preform was taken from the middle of the cross-section in the radial direction and had a cross-sectional area of 6.7 mm × 6.7 mm, 6.7 mm × 7.9 mm and 6.7 mm × 8.6 mm for "high V_f", "mid V_f" and "low V_f" cases, respectively. The analyzed regions, "Region A" and "Region B," taken from the commercial pultruded part, had a cross-sectional area of 6.7 mm × 6.7 mm and were collected from the indicated locations in Figure 1.

Several image processing steps were applied to enhance image processing accuracy. A 2D median filter was used in 5 × 5 pixel subwindows, and the images were binarized with respect to the histogram of the grayscale image. Afterwards, the fibers were detected using Matlab's built-in function ("imfindcircles"), which uses Circular Hough Transform based algorithm to find the circles.[49] An in-house multi-step image processing algorithm eliminated overlapping fibers. Overlapping fibers with a center-to-center distance smaller than half of the larger fiber's radius were considered as a single fiber being detected multiple times. Among the detected overlapping fibers, the one with the higher average pixel intensity was kept, and the other was omitted. Overlapping fibers with a larger center-to-center distance than half of the larger fiber's radius were not deleted but shrunk until the center-to-center distance was equal to 5% of the radius of the larger fiber. This procedure was repeated four times consecutively. Finally, the pixel densities of the detected fibers were rechecked, and any falsely detected fibers were eliminated. A similar multi-step image-processing approach to detect fibers was used in studies by other authors.[50,51]

Some of the most commonly used descriptors, such as the probability distribution of the first-, second-, and third-nearest neighbor distances, were captured for the corresponding cross-sections (see Figure 5B for the schematic representation of the corresponding statistical descriptors). From a permeability perspective, the gap between closer filaments corresponds to the width of the channels between these filaments. Therefore, the shortest distance between the fibers' walls was calculated and presented in this

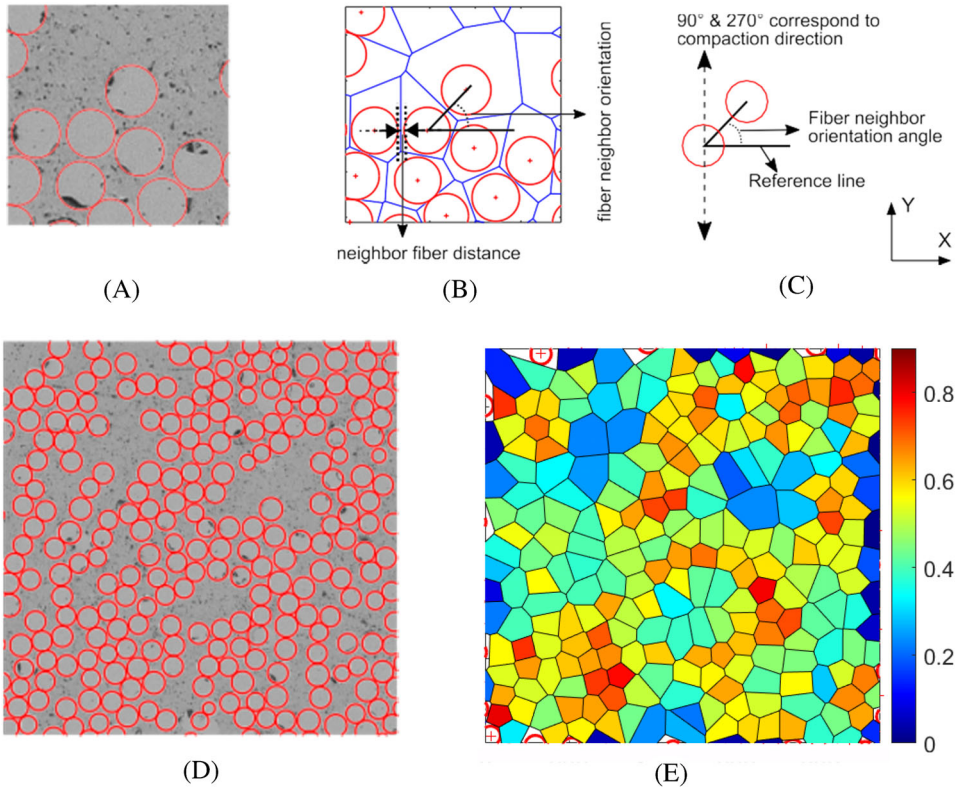

FIGURE 5 Image processing steps; detected fibers (A, D), Voronoi tessellation and statistical descriptors (B), schematic representation of the fiber neighbor orientation and corresponding directions (C), colormap of V_f for the corresponding Voronoi cells (E). Note that this figure is provided with a small domain for illustrative purposes only. The fibers at the domain boundary lead to Voronoi cells that tend towards infinite size, resulting in low fiber volume fractions.[51]

15480569, 0, Downloaded from https://4spepublications.onlinelibrary.wiley.com/doi/10.1002/pc.28171 by Cochrane Netherlands, Wiley Online Library on [22/02/2024]. See the Terms and Conditions (https://onlinelibrary.wiley.com/terms-and-conditions) on Wiley Online Library for rules of use; OA articles are governed by the applicable Creative Commons License

study instead of the center-to-center distance. The bin size was kept constant at 0.5 μm for each probability distribution for a robust comparison. The distribution of the nearest neighbor orientations (see Figure 5C for the schematic representation of the nearest neighbor orientation) was presented to provide information about the spatial distribution and its transformation with compaction.

Voronoi tessellation was used to divide the cross-sectional area into polygons. Each of these polygons contains only one fiber, and there is no closer fiber than the given fiber to the points within that polygon. The probability distribution of the corresponding fiber volume fraction of each Voronoi cell was plotted for the local fiber volume fraction distribution (see Figure 5E). This distribution, therefore, reveals non-uniformity in fiber distribution through the cross-section and the transformation of fiber distribution as compaction increases. The transformation of fiber neighbor distances and orientations was also analyzed to provide valuable information about microstructural transformation. 2D histograms of distance and orientations were plotted for the first-, second-, and third-neighbor fibers to reveal the corresponding transformation of these parameters at increasing compaction levels.

An example of the detected fibers and the representations of the statistical descriptors are seen in Figure 5A–C, respectively. Figure 5D shows an example of a cross-sectional ROI of 448 μm × 448 μm taken from the "low V_f" case and the fibers detected on it. A color map of the local fiber volume fractions, captured using Voronoi tessellation of the corresponding window, is depicted in Figure 5E.

4 | STATISTICAL DESCRIPTORS-BASED MODELS

The link between the non-uniform fiber distribution, which can be analyzed with various statistical descriptors, and permeability has been studied analytically and numerically in the literature, as explained previously. The existing expressions in the literature (see Equations 1–4) were developed using numerical flow simulations for different fibrous domains having distinctive microstructural features. These expressions were employed for the collected cross sections.[23,28,31,32]

-

The statistical descriptors, such as the average nearest fiber distances and orientations, were extracted from the selected ROIs in the investigated cross-sections. Arrays of 15 × 15, 5 × 5, and 3 × 3 ROIs were selected equidistantly over the cross sections of each compaction case. The ROI sizes were respectively equal to 448 μm × 448 μm, 1343 μm × 1343 μm, and 2238 μm × 2238 μm. The estimated apparent permeability values were compared with the experimental results.

5 | RESULTS AND DISCUSSION

5.1 | Experimental measurement of the permeability

Figure 6A shows the experimental results of the permeability measurements. The corresponding permeability levels of each preform were depicted separately with their best fits to Equation (6). The fitting constants for each

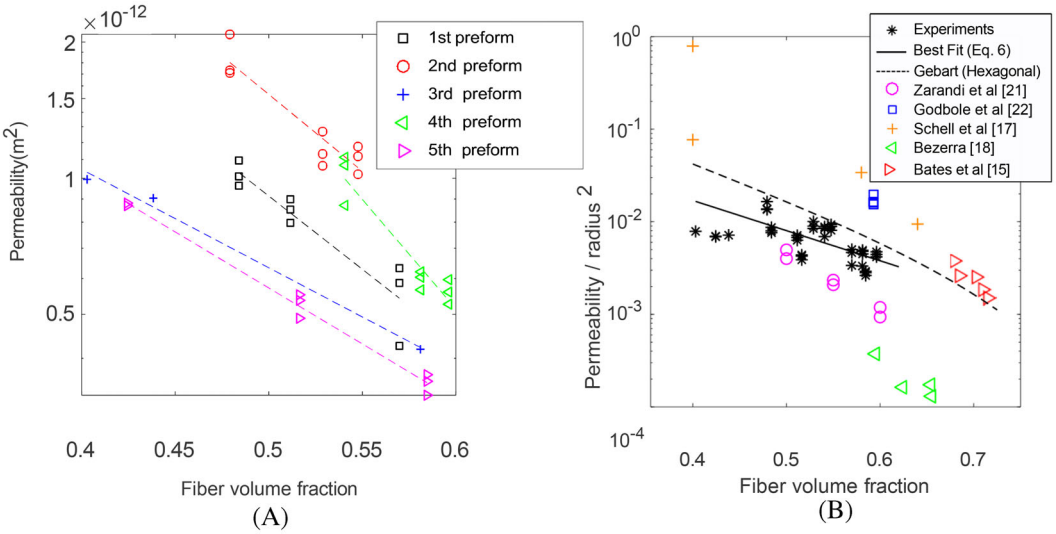

FIGURE 6 The measured permeability values of individual preforms (A). The measured permeability values with the results reported in the literature (B). The equation used for best fit: $K_\perp = C \cdot \exp(-b \cdot V_f)$.

15480569, 0, Downloaded from https://4spepublications.onlinelibrary.wiley.com/doi/10.1002/pc.28171 by Cochrane Netherlands, Wiley Online Library on [22/02/2024]. See the Terms and Conditions (https://onlinelibrary.wiley.com/terms-and-conditions) on Wiley Online Library for rules of use; OA articles are governed by the applicable Creative Commons License

preform, along with the constants for overall data points, are tabulated in Table 1. The slope of the overall fit of the test results was calculated as the average of the slopes of individual preforms. Although a significant scatter is observed between the different preforms, the fitted curves for the change of apparent permeability agree well with Equation (6) for each individual preform in isolation. This can be attributed to the preform-specific microstructural evolution through compaction. It can be hypothesized that the winding process has a strong effect on the initial meso/macro structure of rovings and initial filament distribution. The resulting fiber distribution was close to axisymmetric, which makes the proposed approach suitable for investigating the effect of compaction on transverse permeability.

Figure 6B shows the results of the experiments conducted in this study, together with the experimental transverse permeability values presented in the literature for various UD roving-based fiber beds and Gebart's model in hexagonal packing mode. As the material types, fiber sizes, and methodologies used in these studies varied significantly, said variation is mirrored in the results. Bates et al.[15] measured the permeability of two different types of tows within a compression permeameter. This setup and the methods used can be considered similar to the 1D setup used in the present study. Tows were placed in a rectangular groove, and the reported permeability values are in parallel to the trend of the measured values in the present study, as well as Gebart's hexagonal model for lower porosities such V_f values of 0.7. Werlen et al.[16] confirmed this observation for even higher V_f values (range of 0.77) and validated the analytical model of Gebart with a similar set-up. These observations can be considered reasonable, as uniformity increases in this range of porosities. Zarandi et al.[21] reported relatively similar results as well. In their study, tows were homogeneously placed in a rectangular duct consisting of non-uniformly distributed fibers, while there were no resin-rich layers between tows. This can explain why the permeability values found by Zarandi et al.[21] are generally lower than the results of the present study. Other results depicted in Figure 6B were collected in setups utilizing different principles with regard to flow direction and preform preparation steps. The literature results (see Figure 6B) seem to support our observation that the preparation of the preform influences the reinforcement structure (fiber distribution), and that has a significant effect on the permeability and its variation.

TABLE 1 Fitting constants for Equation (6).

	C (10^{-11}) [m^2]	b [-]	The regression coefficient (R^2)
1st preform	3.80	7.46	0.900
2nd preform	7.64	7.82	0.872
3rd preform	0.78	5.01	0.985
4th preform	41.40	11.15	0.895
5th preform	0.99	5.71	0.991
Overall fit	3.97	7.43	-

5.2 | Fiber distribution quantification in vacuum infused sample

Image analysis of the vacuum-infused samples led to estimated fiber volume fractions of 0.413, 0.470, and 0.532, respectively, for "low V_f", "mid V_f," and "high V_f" cases. This agrees well with the expected fiber volume change at the levels of compaction applied.

The estimated V_f values for the regions captured on the commercial pultruded part (see Figure 1A), i.e., "Region A" and "Region B", were 0.443 and 0.497, respectively.

Voronoi tessellation based color maps of the local fiber volume fractions through the entire cross-sections collected from the vacuum-infused preform are shown in Figure 7A–C. The corresponding color maps for "Region A and B," collected from the pultruded part, are shown in Figure 7D,E. One can see the resin-rich regions in blue and the fiber- dense regions in red. On the cross sections of the vacuum-infused preform, resin-rich regions were formed along the vertical axis (Y-axis, [axial direction]). This observation was in line with the expectations considering the sample preparation technique. On the cross sections collected from the pultruded part, on the other hand, resin-rich cells were accumulated around the rovings without a distinguishable order. Commonly for both of these samples and five of these cross-sections, the amount of resin-rich cells decreased with increasing V_f.

Figure 8A depicts the local fiber volume fraction distribution, which quantitatively illustrates the evolution of uniformity through compaction. The higher number of lower V_f cells in the "low V_f" case indicates that resin-rich cells are more likely to be found in this case. As compaction increases, the probability of lower V_f cells occurring decreases, and the overall distribution narrows. It can be concluded that the dual-scale meso-structure transformed into a more regular micro/meso-structure as compaction increased.

In Figure 8B, the local fiber volume fraction distribution in pultruded part can be seen together with the curves collected from the vacuum infused sample. Overall, the probability distributions in the pultruded part were shifted from "Region A" to "Region B" with increasing V_f similar to the probability distributions captured in the vacuum infused preform.

15480569, 0, Downloaded from https://4spepublications.onlinelibrary.wiley.com/doi/10.1002/pc.28171 by Cochrane Netherlands, Wiley Online Library on [22/02/2024]. See the Terms and Conditions (https://onlinelibrary.wiley.com/terms-and-conditions) on Wiley Online Library for rules of use; OA articles are governed by the applicable Creative Commons License

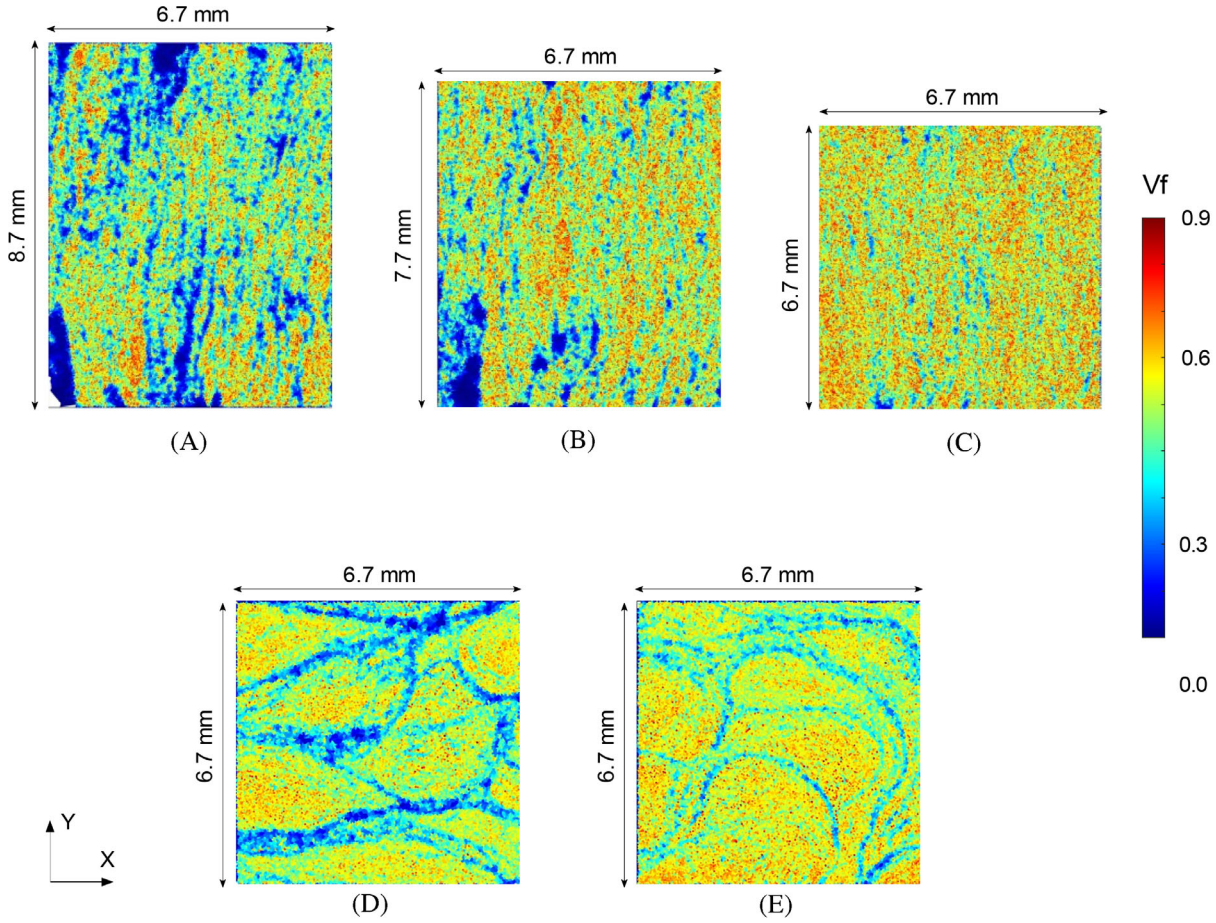

FIGURE 7 Full field views of the analyzed cross-sections collected from vacuum infused sample; "Low V_f" ($V_f = 0.413$) (A), "Mid V_f" ($V_f = 0.470$) (B), "High V_f" ($V_f = 0.532$) (C). The analyzed cross-sections collected from the pultruded part are shown in Figure 1; "Region A" ($V_f = 0.443$) (D), "Region B" ($V_f = 0.497$) (E).

While the probability distributions of lower V_f cells were similar in both vacuum infused preform and the pultruded part, the probability of observing high V_f cell (more than 60%) in the pultruded part was lower than in the vacuum-infused preform. This observed discrepancy is suspected to originate from differences in preliminary steps in pultrusion (like tow spreading etc.), and the compaction characteristics. In the case of the commercial part, the rovings experience a reduction of available space in both the x and y axes simultaneously due to the nature of the pultrusion process. The gradually evolving cross sections result in a rather uniform fiber volume fraction. In contrast, the vacuum-infused preform is wound around the y direction only. Thus, the rovings tend to exhibit an elliptical cross section whose major axis is aligned with the y direction. Consequently, although fiber arrangement is more regular, applying compaction in only one direction maintains oriented resin-rich areas between the rovings and results in a wider distribution compared to the pultruded specimen.

Figure 9A shows the first, second, and third nearest fiber distance distributions for each level of compaction. In general, as compaction increases, the distribution curves are constricted with more prominent peaks. The negligible difference between the first nearest neighbor distribution of "low, mid, and high V_f" cases might be related to the number of fibers that are almost touching. Figure 9B shows the same distributions for "Region A" and "Region B." In the pultruded part, peaks of the curves moved to the right compared to the curves collected from the vacuum-infused preform. This trend showed that the occurrence of closer fibers in pultruded part was much lower than in the vacuum- infused preform. This result is in line with the higher V_f cell probability in the pultruded part being lower than in the vacuum-infused preform as discussed above. On the other hand, the evolution of curves with the increasing V_f was quite similar in both the vacuum-infused preform and the pultruded part.

Figure 9C shows the change in the first nearest neighbor orientation distribution in a polar plot with increasing levels of compaction. The angular distribution of "low V_f" shows that the nearest neighbor fibers were slightly accumulated at 0°, 90°, 180°, 270°, and

15480569, 0, Downloaded from https://4spepublications.onlinelibrary.wiley.com/doi/10.1002/pc.28171 by Cochrane Netherlands, Wiley Online Library on [22/02/2024]. See the Terms and Conditions (https://onlinelibrary.wiley.com/terms-and-conditions) on Wiley Online Library for rules of use; OA articles are governed by the applicable Creative Commons License

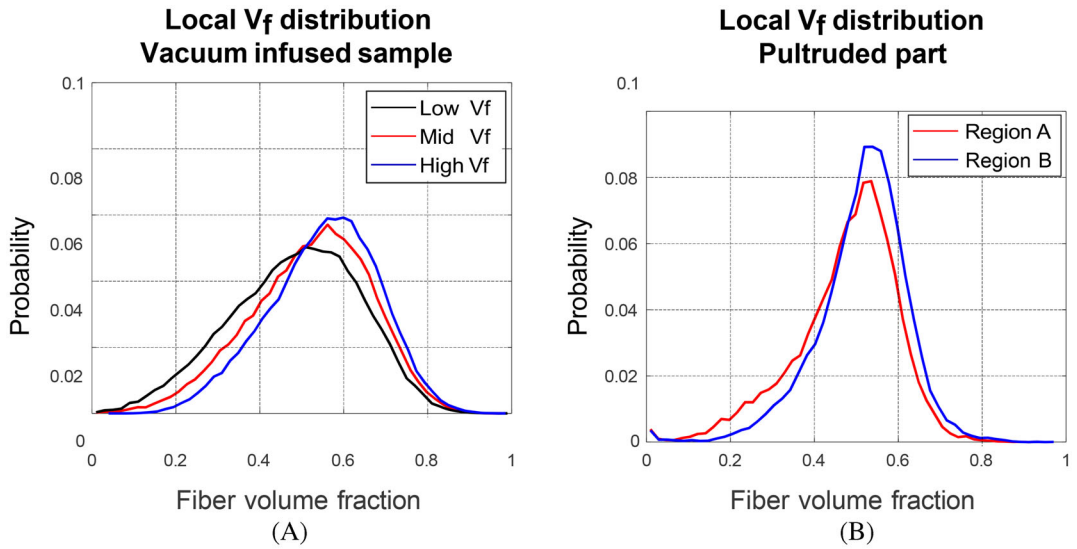

FIGURE 8 Local V_f distribution based on the corresponding fiber volume fractions of Voronoi cells; collected from the vacuum-infused sample (A), collected from the pultruded part (B). The bin size is 0.02.

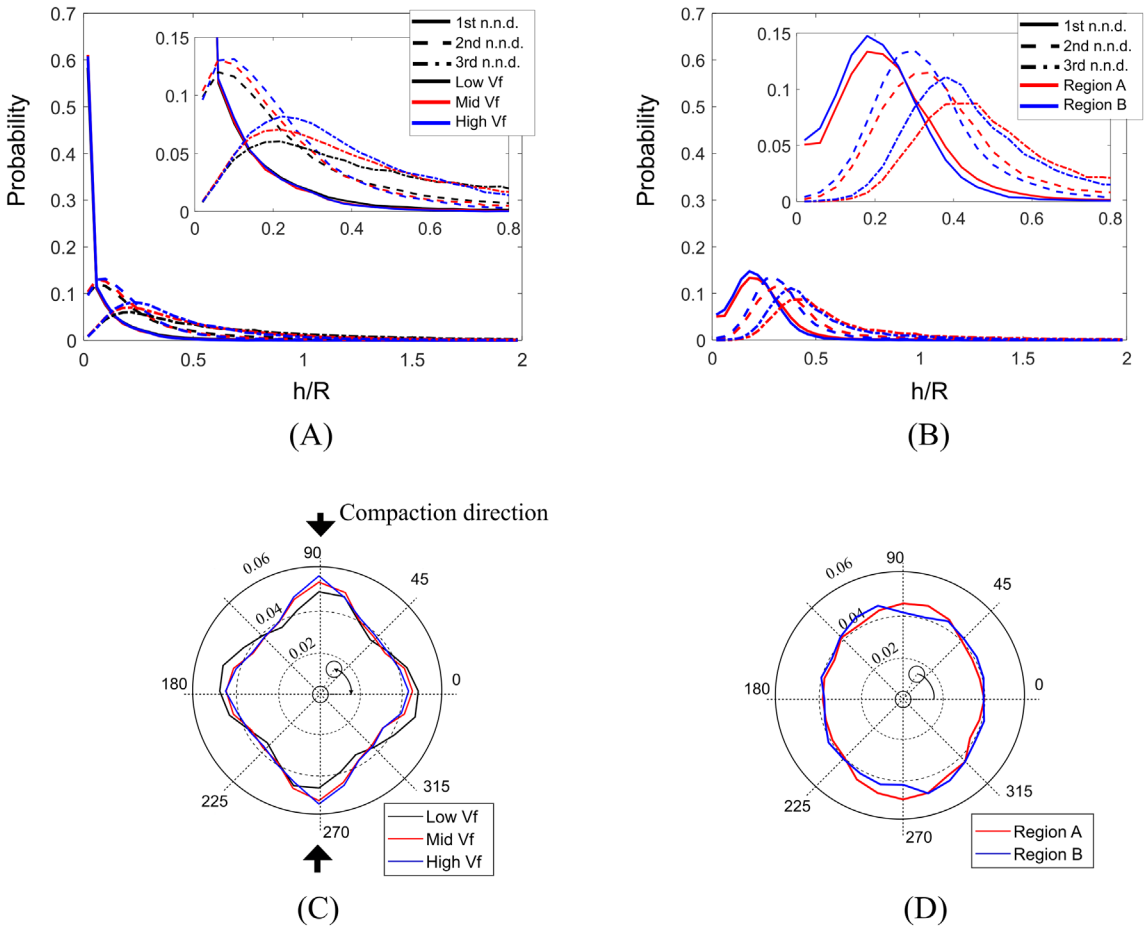

FIGURE 9 Probability distribution of the first, second, and third normalized nearest neighbor distance (n.n.d.); collected from the vacuum-infused sample (A), collected from the pultruded part (B) (The distance (h) is normalized with the average radius (r) in these distributions). Orientation angle probability distribution for the first neighbor fibers (distance of a data point to the origin indicates the probability); collected from the vacuum-infused sample (C), collected from the pultruded part (D).

15480569, 0, Downloaded from https://4spepublications.onlinelibrary.wiley.com/doi/10.1002/pc.28171 by Cochrane Netherlands, Wiley Online Library on [22/02/2024]. See the Terms and Conditions (https://onlinelibrary.wiley.com/terms-and-conditions) on Wiley Online Library for rules of use; OA articles are governed by the applicable Creative Commons License

360°. This formation can be attributed to the preparation steps of the preform, as winding induces compaction in the radial direction (*X* direction), which corresponds to accumulation at 0°, 180°, and 360°. As compaction increased, fiber accumulation along the compaction direction (corresponds to 90° and 270°) intensified. The nearest neighbor orientation distribution in the pultruded part, depicted in Figure 9D, showed a weaker directional accumulation along only the vertical direction (*Y* direction). This can be attributed to the processing conditions, more specifically to the horizontal pins used for guiding and spreading rovings that causes a preferential accumulation of filaments in the rovings and thus a lack of symmetry in the subsequent compaction characteristics.

The fiber distribution statistics comparison between the vacuum-infused sample and the pultruded part ("Region A" and "Region B") showed that the created microstructure by means of the method presented in this study can be considered similar to the pultruded part's cross-sections with slightly distinctive characteristics. The nearest neighbor distributions revealed that the observed distances between nearest neighbors were slightly longer in "Regions A and B" compared to the vacuum-infused samples. This can be an indicator of some amount of fiber spreading by mechanical means or hydrodynamic effects for the commercial pultruded part. Fiber spreading was not applied to the roving while preparing the vacuum-infused preform, which can be commented to result in a higher probability of closer fibers. The directional distributions revealed that the evolution and the current state of the fiber distribution were dependent on the initial state of the preform and the compaction.

Apart from the individual statistical descriptors of fiber distribution, the coupled representation of the distance and the neighbor orientation is also essential to understand structural evolution through compaction. As compaction increases, the fibers undergo direction dependent reorganization, as observed in Figure 10C, supporting the results presented in Reference 26. Figure 10 shows the 2D histogram of fiber neighbor distance and fiber neighbor orientation. The glass and aluminum molds induce compaction in the *Y* direction (axial direction), which corresponds to 90° and 270° in this figure. As shims were added, compaction increased, and accumulation in these directions became more prominent, decreasing the relative length of channels in the compaction direction between neighbor fibers. Figure 10A–C depict the 2D histograms of

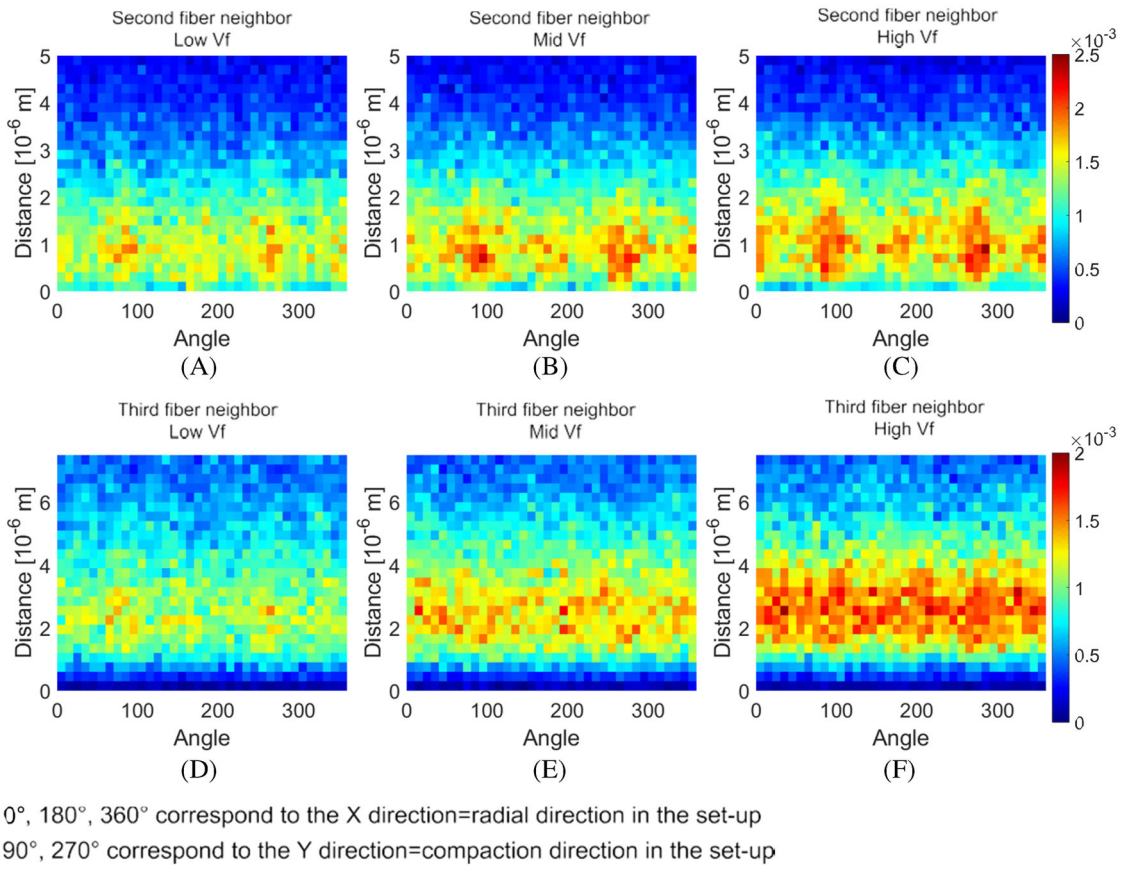

FIGURE 10 2D histograms of the second fiber neighbor distance and orientations in "Low V_f," "Mid V_f," and "High V_f" cases (A–C). 2D histograms of the third fiber neighbor distance and orientations in "Low V_f", "Mid V_f," and "High V_f" cases (D–F).

15480569, 0, Downloaded from https://4spepublications.onlinelibrary.wiley.com/doi/10.1002/pc.28171 by Cochrane Netherlands, Wiley Online Library on [22/02/2024]. See the Terms and Conditions (https://onlinelibrary.wiley.com/terms-and-conditions) on Wiley Online Library for rules of use; OA articles are governed by the applicable Creative Commons License

the second fiber neighbors, revealing that the channels between fibers and their second closest neighbors accumulated around 90° and 270°, while shorter channels became more prevalent. A possible consequence of this directional distribution is that flow resistance may increase in the X direction (radial direction), which may result in anisotropic transverse permeability. For the third fiber neighbor distribution, which is shown in Figure 10D–F, there was no directional accumulation, while the number of smaller gaps still increased with further compaction.

The microstructural analysis conducted in this study revealed the presence of an anisotropic fiber distribution in the tested preforms at both the meso- and micro-levels. Figure 8A–C illustrates the meso-level anisotropy induced by the preparation technique, which resulted in vertically aligned inter-roving regions (i.e., formed along the flow direction). Through the compaction process, these inter-roving regions disappeared, leading to an increase in the occurrence of vertically aligned neighbor fibers, thus exhibiting micro-level anisotropy (see Figures 9A and 10). Both of these mechanisms contribute to an increase in permeability in the direction of the test. Consequently, the experimental results presented in this study can be considered as an upper boundary for the transverse permeability of the investigated roving-based system.

5.3 | Numerically estimated local permeability values and their comparison with the experimental results

Figure 11 shows the predicted permeability values according to Gebart's,[23] Chen's,[31] Yazdchi's,[28] and Gommer's[32] models through the investigated cross-sections. The smallest ROI size presented in this study is equal to 448 μm × 448 μm, which corresponds to an edge length of almost 40 times the average fiber radius. This ROI size is larger than the RVEs used for the development of these statistical models. Figure 11A illustrates the results for the smallest ROI size for each V_f case. It can be seen that each model provided a consistent trend within each V_f case. Figure 11B depicts the results for each ROI size. It is worth noting that the models were used with the coefficients proposed in their original studies and the statistical parameters captured in the present study. Readers can refer to the study of Gommer et al.[32] for a similar comparison using the artificially generated statistically representative microstructures.

As shown in Figure 11, Gommer's model showed distinctive behavior, especially for lower fiber volume fractions. This can be caused by the fact that Gommer's model (Equation 4) was developed by fitting CFD simulations solved in high V_f RVEs (0.63–0.74),[32] preventing a proper generalization to low V_f RVEs. Both Chen's and Yazdchi's models produced lower permeability values than Gebart's hexagonal and quadratic models. The slopes of Yazdchi's model (Equation 3) and Gebart's model for the hexagonal packing (Equation 1), however, were closer to each other, with the former using average second fiber neighbor distance and radius and the latter using V_f and radius. The slope of Gebart's model for the quadratic packing and Chen's model (Equation 2), which depends on the first fiber neighbor distance, were slightly different than the others. Due to higher variability in the second fiber distance, Yazdchi's model resulted in more scattered data.

In Figure 12, the measured permeability values are compared with the estimated permeability values using previously proposed expressions. The general trend suggests that the experimental results are higher than the predictions of Yazdchi's and Chen's models and lower than those of Gebart's model for the hexagonal packing. Regards to the link between permeability and fiber volume fraction, the experimental results show a similar trend as Gebart's hexagonal and Yazdchi's models. This

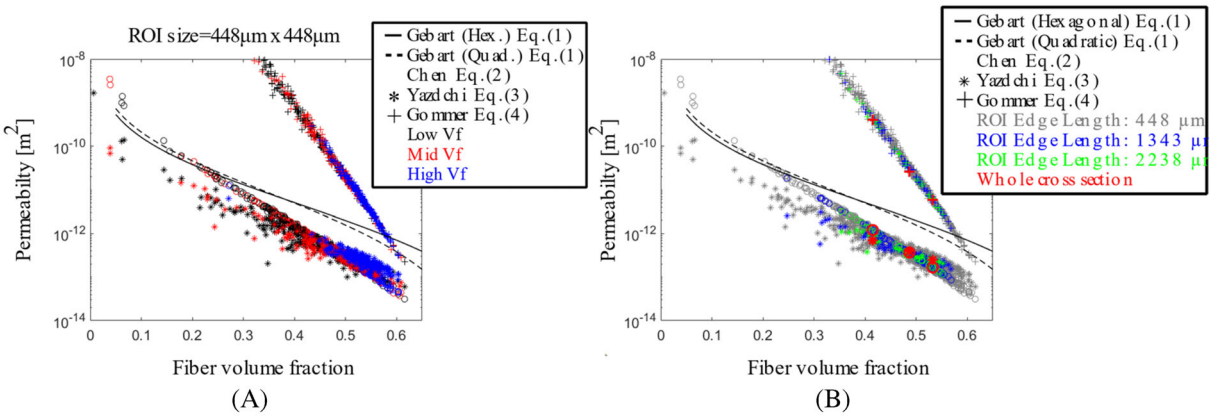

FIGURE 11 Permeability estimations based on the available models in the literature which relates the apparent permeability with the statistical descriptors.

15480569, 0, Downloaded from https://4spepublications.onlinelibrary.wiley.com/doi/10.1002/pc.28171 by Cochrane Netherlands, Wiley Online Library on [22/02/2024]. See the Terms and Conditions (https://onlinelibrary.wiley.com/terms-and-conditions) on Wiley Online Library for rules of use; OA articles are governed by the applicable Creative Commons License

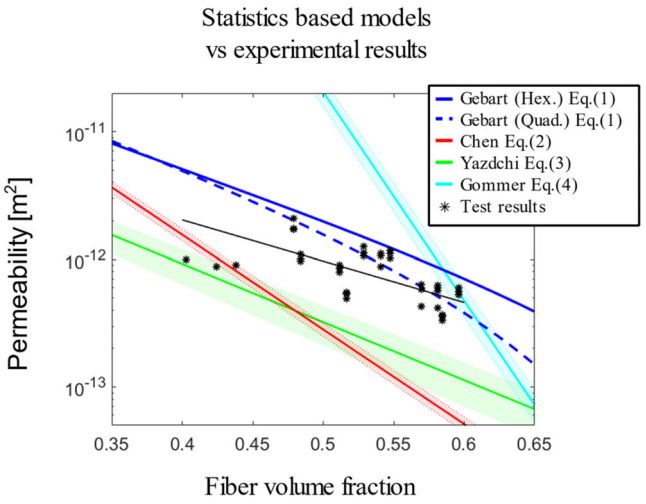

FIGURE 12 Comparison between the numerically predicted values calculated with the currently available models and the measured permeability values.

similarity in trend shows that the statistics-based permeability expressions are promising to capture the variability in permeability within the flow domain. However, it is worth noting that the currently available models do not take transverse anisotropy into account. The investigated cross-sections and the statistical analysis in the present study showed that local and global transverse anisotropy can also be expected with resin-rich layers, i.e., inter-tow regions, depending on the preparation technique and processing. Therefore, further modeling approaches and statistics-based expressions taking anisotropy into account are recommended.

6 | CONCLUSIONS

In order to model flow phenomena during pultrusion, the apparent permeability of roving-based systems is required. Quantifying the permeability of roving-based systems is more challenging than for fabrics due to their lack of structural integrity. In this study, we developed an experimental procedure for measuring the transverse permeability of roving-based preforms. We compared the results with those of similar studies and showed that they were in line with the results obtained using similar setups.

The micro/meso-structure and its evolution during processing is another important aspect in understanding the fundamentals of flow behavior in pultrusion and further liquid composite molding techniques. To investigate the microstructural evolution, a similar preform as the tested preform was produced with vacuum infusion. The changes in the fiber distribution due to compaction were investigated by utilizing filament-level statistical descriptors. The results showed that uniformity increases with compaction, as expected. Orientational accumulation of the nearest fiber neighbors was observed parallel to the direction of compaction, which reveals a processing effect that should be taken into account during modeling.

Numerical permeability estimation techniques were applied to explore the influence of processing/compaction on apparent permeability. Various previously developed expressions were used on the ROIs captured in the experiment. Models based on statistical descriptors produced reasonably good estimations. It must be noted, however, that these expressions were developed in virtually generated ROIs, as is common in the literature. Random or statistical microstructure generation may conceal the effects of preparation and processing/compaction on the microstructure and its evolution. The currently available statistical models are limited in terms of accounting for the inherently anisotropic permeability commonly encountered during the impregnation of roving-based systems. A comprehensive approach is still needed to predict the apparent transverse permeability of a fiber bed with anisotropy induced by resin-rich layers. It will be of interest to combine virtual fiber modeling[52] with flow models in a multiphysics modeling framework in future work.

Experimental analysis of the transverse permeability of the most commonly used roving types leads to more accurate process modeling of pultrusion or similar liquid composite molding techniques. The link between statistical descriptors of fiber distribution and compaction paves the way to reveal the effect of processing not only on permeability but also on the structural analysis of composites.

ACKNOWLEDGMENTS

This work is part of the project named "Modeling the multi-physics in RIP of complex industrial profiles" which has been granted by the Danish Council for Independent Research | Technology and Production Sciences (DFF/FTP), grant number: DFF-6111-00112. We acknowledge the Swiss National Science Foundation (SNF-182669) for financial support.

CONFLICT OF INTEREST STATEMENT

The authors declare no conflicts of interest.

DATA AVAILABILITY STATEMENT

Data available on request from the authors.

ORCID

Onur Yuksel https://orcid.org/0000-0002-9843-2674
Véronique Michaud https://orcid.org/0000-0001-5699-740X

REFERENCES

1. Volk M, Yuksel O, Baran I, Hattel JH, Spangenberg J, Sandberg M. Cost-efficient, automated, and sustainable composite profile manufacture: a review of the state of the art,

15480569, 0, Downloaded from https://4spepublications.onlinelibrary.wiley.com/doi/10.1002/pc.28171 by Cochrane Netherlands, Wiley Online Library on [22/02/2024]. See the Terms and Conditions (https://onlinelibrary.wiley.com/terms-and-conditions) on Wiley Online Library for rules of use; OA articles are governed by the applicable Creative Commons License

innovations, and future of pultrusion technologies. *Compos Part B: Eng*. 2022;246:110135.

2. Sandberg M, Yuksel O, Comminal RB, et al. 6 – numerical modeling of the mechanics of pultrusion. In: Silberschmidt VV, ed. *Mechanics of Materials in Modern Manufacturing Methods and Processing Techniques Elsevier Series in Mechanics of Advanced Materials*. Elsevier; 2020:173-195.
3. Sandberg M, Yuksel O, Baran I, Hattel JH, Spangenberg J. Numerical and experimental analysis of resin-flow, heat-transfer, and cure in a resin-injection pultrusion process. *Compos Part A: Appl Sci Manuf*. 2021;143:106231.
4. Tucci F, Bezerra R, Rubino F, Carlone P. Multiphase flow simulation in injection pultrusion with variable properties. *Mater Manuf Process*. 2020;35(2):152-162.
5. Yuksel O, Sandberg M, Baran I, Ersoy N, Hattel JH, Akkerman R. Material characterization of a pultrusion specific and highly reactive polyurethane resin system: elastic modulus, rheology, and reaction kinetics. *Compos Part B: Eng*. 2021;207:108543.
6. Tian L, Zhang P, Xian G. An acrylic resin system for in-situ pultrusion: curing performances and rheology. *Polym Compos*. 2023;45:243-255.
7. Yuksel O, Sandberg M, Hattel JH, Akkerman R, Baran I. Meso-scale process modeling of a thick pultruded composite with variability in fiber volume fraction. *Materials*. 2021;14(13):3763.
8. Feng P, Wu Y, Liu T. Non-uniform fiber-resin distributions of pultruded GFRP profiles. *Compos Part B: Eng*. 2022;231:109543.
9. Vedernikov A, Gemi L, Madenci E, et al. Effects of high pulling speeds on mechanical properties and morphology of pultruded GFRP composite flat laminates. *Compos Struct*. 2022;301:116216.
10. Baran I, Straumit I, Shishkina O, Lomov SV. X-ray computed tomography characterization of manufacturing induced defects in a glass/polyester pultruded profile. *Compos Struct*. 2018;195:74-82.
11. Arbter R, Beraud J, Binetruy C, et al. Experimental determination of the permeability of textiles: a benchmark exercise. *Compos Part A: Appl Sci Manuf*. 2011;42(9):1157-1168.
12. Vernet N, Ruiz E, Advani S, et al. Experimental determination of the permeability of engineering textiles: benchmark II. *Compos Part A: Appl Sci Manuf*. 2014;61:172-184.
13. May D, Aktas A, Advani S, et al. In-plane permeability characterization of engineering textiles based on radial flow experiments: a benchmark exercise. *Compos Part A: Appl Sci Manuf*. 2019;121:100-114.
14. Yong A, Aktas A, May D, et al. Out-of-plane permeability measurement for reinforcement textiles: a benchmark exercise. *Compos Part A: Appl Sci Manuf*. 2021;148:106480.
15. Bates PJ, Taylor D, Cunningham MF. Compaction and transverse permeability of glass rovings. *Appl Compos Mater*. 2001;8(3):163-178.
16. Werlen V, Vocke R, Brauner C, Dransfeld C, Michaud V, Rytka C. A model for the consolidation of hybrid textiles considering air entrapment, dissolution and diffusion. *Compos Part A: Appl Sci Manuf*. 2023;166:107413.
17. Schell JSU, Siegrist M, Ermanni P. Experimental determination of the transversal and longitudinal fibre bundle permeability. *Appl Compo Mater*. 2007;14(2):117-128.
18. Bezerra R. Modelling and Simulation of the Closed Injection Pultrusion Process. PhD thesis. Karlsruher Institut für Technologie (KIT). 2017.
19. Sandberg M, Kabachi A, Volk M, et al. Permeability and compaction behaviour of air-texturised glass fibre rovings: a characterisation study. *J Compos Mater*. 2020;54(27):4241-4252.
20. Wu X, Li J, Shenoi RA. A new method to determine fiber transverse permeability. *J Compos Mater*. 2007;41(6):747-756.
21. Zarandi MAF, Arroyo S, Pillai KM. Longitudinal and transverse flows in fiber tows: evaluation of theoretical permeability models through numerical predictions and experimental measurements. *Compos Part A: Appl Sci Manuf*. 2019;119:73-87.
22. Godbole MG, Purandare R, Harshe R, et al. Influence of filament distribution on transverse tow permeability: model predictions and experimental validation. *Compos Part A: Appl Sci Manuf*. 2019;118:150-161.
23. Gebart B. Permeability of unidirectional reinforcements for RTM. *J Compos Mater*. 1992;26(8):1100-1133.
24. Vaughan T, McCarthy C. A combined experimental–numerical approach for generating statistically equivalent fibre distributions for high strength laminated composite materials. *Compos Sci Technol*. 2010;70(2):291-297.
25. Romanov V, Lomov SV, Swolfs Y, Orlova S, Gorbatikh L, Verpoest I. Statistical analysis of real and simulated fibre arrangements in unidirectional composites. *Compos Sci Technol*. 2013;87:126-134.
26. Gommer F, Endruweit A, Long A. Analysis of filament arrangements and generation of statistically equivalent composite micro-structures. *Compos Sci Technol*. 2014;99:45-51.
27. Gomarasca S, Peeters D, Atli-Veltin B, Dransfeld C. Characterising microstructural organisation in unidirectional composites. *Compos Sci Technol*. 2021;215:109030.
28. Yazdchi K, Srivastava S, Luding S. Micro–macro relations for flow through random arrays of cylinders. *Compos Part A: Appl Sci Manuf*. 2012;43(11):2007-2020.
29. Bodaghi M, Catalanotti G, Correia N. On the statistics of transverse permeability of randomly distributed fibers. *Compos Struct*. 2016;158:323-332.
30. Bechtold G, Ye L. Influence of fibre distribution on the transverse flow permeability in fibre bundles. *Compos Sci Technol*. 2003;63(14):2069-2079.
31. Chen X, Papathanasiou TD. The transverse permeability of disordered fiber arrays: a statistical correlation in terms of the mean nearest interfiber spacing. *Trans Porous Media*. 2008;71(2):233-251.
32. Gommer F, Endruweit A, Long AC. Influence of the microstructure on saturated transverse flow in fibre arrays. *J Compos Mater*. 2018;52(18):2463-2475.
33. Huang W, Causse P, Hu H, Trochu F. Numerical and experimental investigation of saturated transverse permeability of 2D woven glass fabrics based on material twins. *Polym Compos*. 2020;41(4):1341-1355.
34. Lam RC, Kardos JL. The permeability and compressibility of aligned and cross-plied carbon fiber beds during processing of composites. *Polym Eng Sci*. 1991;31(14):1064-1070.
35. Endruweit A, Luthy T, Ermanni P. Investigation of the influence of textile compression on the out-of-plane permeability of a bidirectional glass fiber fabric. *Polym Compos*. 2002;23(4):538-554.

15480569, 0, Downloaded from https://4spepublications.onlinelibrary.wiley.com/doi/10.1002/pc.28171 by Cochrane Netherlands, Wiley Online Library on [22/02/2024]. See the Terms and Conditions (https://onlinelibrary.wiley.com/terms-and-conditions) on Wiley Online Library for rules of use; OA articles are governed by the applicable Creative Commons License

36. Han K, Lee C, Rice BP. Measurements of the permeability of fiber preforms and applications. *Compos Sci Technol*. 2000; 60(12):2435-2441.
37. Fauster E, Vierkötter C, Appel L, Lugo J, Schijve W, Heider D. Experimental characterization of single ply out-of-plane permeability through gaseous flow. *Polym Compos*. 2018;39(9):3247-3258.
38. Trindade RS, Ribeiro AC, Souza JA, Amico SC. Experimental investigation of transverse permeability applied to liquid molding. *Polym Compos*. 2019;40(10):3938-3946.
39. Scholz S, Gillespie JW, Heider D. Measurement of transverse permeability using gaseous and liquid flow. *Compos Part A: Appl Sci Manuf*. 2007;38(9):2034-2040.
40. Konstantopoulos S, Grössing H, Hergan P, Weninger M, Schledjewski R. Determination of the unsaturated through-thickness permeability of fibrous preforms based on flow front detection by ultrasound. *Polym Compos*. 2018;39(2): 360-367.
41. Kabachi M, Stettler L, Arreguin S, Ermanni P. Concurrent characterization of through-thickness permeability and compaction of fiber reinforcements. *Compos Part A: Appl Sci Manuf*. 2021;141:106203.
42. Merhi D, Michaud V, Kämpfer L, Vuilliomenet P, Månson JAE. Transverse permeability of chopped fibre bundles with an elliptical cross-section. *Compos Part A: Appl Sci Manuf*. 2007;38(3):739-746.
43. Ouagne P, Bréard J. Continuous transverse permeability of fibrous media. *Compos Part A: Appl Sci and Manuf*. 2010;41(1):22-28.
44. Klunker F, Danzi M, Ermanni P. Fiber deformation as a result of fluid injection: modeling and validation in the case of saturated permeability measurements in through thickness direction. *J Compos Mater*. 2015;49(9):1091-1105.
45. Yang B, Huang W, Causse P, Béguin C, Wang J, Trochu F. On the design of test molds based on unidirectional saturated flows to measure transverse permeability in liquid composite molding. *Polym Compos*. 2022;43(4):2234-2251.
46. van de Ven EC, Loendersloot R, Akkerman R. Experimental investigation of the compressibility and permeability of fabric reinforcements. In *Proceedings of the 8th International Conference on Flow Process in Composite Material (FPCM)*, Ecole des Mines de Douai; 2006:241-248..
47. Caglar B, Orgéas L, Rolland du Roscoat S, Sozer EM, Michaud V. Permeability of textile fabrics with spherical inclusions. *Compos Part A: Appl Sci Manuf*. 2017;99:1-14.
48. Salvatori D, Caglar B, Teixidó H, Michaud V. Permeability and capillary effects in a channel-wise non-crimp fabric. *Compos Part A: Appl Sci Manuf*. 2018;108:41-52.
49. The Mathworks, Inc., Natick, Massachusetts. MATLAB version 9.7.0.1216025 (R2019b) Update 1. 2019.
50. Sanei SHR, Barsotti EJ, Leonhardt D, Ray S, Fertig I. Characterization, synthetic generation, and statistical equivalence of composite microstructures. *J Compos Mater*. 2017;51(13):1817-1829.
51. Katuin N, Peeters DMJ, Dransfeld CA. Method for the microstructural characterisation of unidirectional composite tapes. *J Compos Sci*. 2021;5(10):275.
52. Daelemans L, Tomme B, Caglar B, et al. Kinematic and mechanical response of dry woven fabrics in through-thickness compression: virtual fiber modeling with mesh overlay technique and experimental validation. *Compos Sci Technol*. 2021; 207:108706.

How to cite this article: Yuksel O, Caglar B, Broggi G, Michaud V, Akkerman R, Baran I. Saturated transverse permeability of unidirectional rovings for pultrusion: The effect of microstructural evolution through compaction. *Polym Compos*. 2024;1-18. doi:10.1002/pc.28171

15480569, 0, Downloaded from https://4spepublications.onlinelibrary.wiley.com/doi/10.1002/pc.28171 by Cochrane Netherlands, Wiley Online Library on [22/02/2024]. See the Terms and Conditions (https://onlinelibrary.wiley.com/terms-and-conditions) on Wiley Online Library for rules of use; OA articles are governed by the applicable Creative Commons License